RSC Advances

PAPER

View Article Online
View Journal | View Issue

Cite this: *RSC Adv.*, 2024, **14**, 25571

Preparation of $Zn_3Nb_2O_8$ anode material for high-performance lithium/sodium-ion batteries†

Xuemin Yin, *[a] Shuling Cheng,[b] Yuyang Zhang[c] and Chencheng Liu[a]

Niobium-based oxides (M-Nb-O) as promising lithium/sodium-ion storage anode materials have attracted much attention. More types of niobium-based oxides are prepared in order to provide more candidates for anode materials. Herein, $Zn_3Nb_2O_8$ as a novel intercalation-type anode material has been reported for the first time. Arborescent $Zn_3Nb_2O_8$ particles ($Zn_3Nb_2O_8$-A) and stump-like $Zn_3Nb_2O_8$ particles ($Zn_3Nb_2O_8$-B) have been prepared by solid-state and solvothermal methods, respectively. Benefiting from the microsized stump-like structure and the exposure of the (110) facet, $Zn_3Nb_2O_8$-B delivers superior long-term cycling stability with a 139.6% capacity retention (291.8 mA h g^{-1}) over 650 cycles at 0.5 A g^{-1} and a large reversible specific capacity of 91.4 mA h g^{-1} at 4.0 A g^{-1} in lithium-ion batteries. Furthermore, the $Zn_3Nb_2O_8$-B electrode exhibits outstanding cycling stability (100.1 mA h g^{-1} with 94.5% capacity retention after 400 cycles at 0.5 A g^{-1}) in sodium-ion batteries. The excellent electrochemical performance of the stump-like $Zn_3Nb_2O_8$-B materials can be attributed to the exposure of the (110) facet, enlarged interlayer spacing, small charge transfer resistance, and high pseudocapacitive contribution. Therefore, $Zn_3Nb_2O_8$-B has great application prospects as an anode material for lithium/sodium-ion storage.

Received 17th May 2024
Accepted 2nd July 2024

DOI: 10.1039/d4ra03616f

rsc.li/rsc-advances

1 Introduction

The development of electronics, electric vehicles, and smart grids has created a huge demand for lithium-ion batteries (LIBs) with high energy density, long cycle life, and low cost.[1–3] As an important part of LIBs, anode materials should have the characteristics of high specific capacity and excellent cycle performance. Although the existing intercalation material technology has matured, the problem of slow diffusion kinetics of Li^+ in graphite cannot be avoided, which limits the development and application of LIBs in the field of fast charging. Therefore, anode materials with the advantages of high rate and long life are an effective method to solve the above problems.

In recent years, niobium-based oxides have been found to exhibit stable Wadsley–Roth phases with shear-type crystal structures, fast ion intercalation and deintercalation, excellent rate capability, and high operating voltages (above 1.0 V). Therefore, niobium-based oxides have become very promising candidates for electrochemical energy storage materials. The M in binary niobium-based oxides (M-Nb-O) generally includes elements such as Sn,[4] Fe,[5] Zn,[6,7] Ti,[8,9] W,[10,11] Mo,[12,13] Cr,[14,15] Ge,[16] Ga,[17] V,[18] Mg,[19] P[20] or Ni,[21,22] which can provide more redox electron pairs and make the overall structure of niobium-based materials have higher energy density and theoretical capacity. Therefore, the application of M-Nb-O type anode materials in LIBs has recently attracted extensive attention.

Zinc has the advantages of light weight, relatively cheap price and the large ionic radius of Zn^{2+} (0.740 Å), which can provide a wider transport channel for Li^+ and improve the diffusion rate of Li^+. Therefore, zinc niobium oxide has great advantages as an energy storage material. At present, there are few reports on zinc niobium oxide as an electrode material, mainly involving $ZnNb_2O_6$,[6] $Zn_2Nb_{34}O_{87}$.[7] For example, bulk-$ZnNb_2O_6$ materials were successfully prepared by solid-state reaction and showed stable electrochemical performance in LIBs (specific capacity of 181.9 mA h g^{-1} after 100 cycles at 0.1 A g^{-1}).[6] Zhu's group successfully prepared $Zn_2Nb_{34}O_{87}$ blocks by a solid-state reaction method and used them as anode materials for LIBs, which showed excellent cycling performance (216.5 mA h g^{-1} after 100 cycles at 0.4 A g^{-1}).[7] It can be seen that the different proportions of Zn, Nb and O elements will affect the electrochemical properties of Zn–niobium oxide anode materials. Moreover, the $Zn_3Nb_2O_8$ materials and their applications as anode materials in lithium/sodium-ion batteries have yet to be investigated. Based on the above research results and related literature research, we have not found any literature on $Zn_3Nb_2O_8$ as an anode material and its application in lithium/sodium-ion batteries.

Herein, we prepared two $Zn_3Nb_2O_8$ materials with distinct morphologies through different methods and the $Zn_3Nb_2O_8$

[a]Hebei Key Laboratory of Green Development of Rock and Mineral Materials, Hebei GEO University, Shijiazhuang 050031, China. E-mail: xueminyin24@163.com
[b]School of Chemical and Environmental Engineering, Shanghai Institute of Technology, Shanghai 201418, China
[c]Faculty of Robot Science and Engineering, Northeastern University, Liaoning 110819, China

† Electronic supplementary information (ESI) available. See DOI: https://doi.org/10.1039/d4ra03616f

was used as the electrode material in lithium/sodium-ion batteries for the first time. Arborescent $Zn_3Nb_2O_8$ particles ($Zn_3Nb_2O_8$-A) with a size ranging from 300 to 2300 nm were fabricated *via* a conventional solid-state reaction (Fig. 1a), and stump-like $Zn_3Nb_2O_8$ particles ($Zn_3Nb_2O_8$-B) with a size ranging from 250 to 1700 nm were fabricated through a solvothermal method (Fig. 1b). The morphological characteristics, crystalline structure, chemical composition and electrochemical performance of these two $Zn_3Nb_2O_8$ materials were systematically investigated. Compared with $Zn_3Nb_2O_8$-A, $Zn_3Nb_2O_8$-B exhibited good rate performance (reversible capacity of 91.4 mA h g^{-1} at 4.0 A g^{-1}) and excellent cycling stability (291.8 mA h g^{-1} after 650 cycles at 0.5 A g^{-1}). Therefore, $Zn_3Nb_2O_8$-B is expected to be a promising electrode material in the future.

2 Experimental

2.1 Material preparation

According to the traditional solid-phase synthesis method,[23,24] 3.0 mmol of zinc oxide (ZnO, 99.99%, Macklin) and 1.0 mmol of niobium pentoxide (Nb_2O_5, 99.9%, Aladdin) were added to absolute ethanol, and mixed uniformly under the action of a ball mill (Fig. 1a). The mixed solution after ball milling was dried in a blast drying oven at 80 °C for 12 h to obtain a white powdery precursor. Finally, the precursor was calcined at a heating rate of 5 or 10 °C min^{-1} for 2 hours in an air or argon atmosphere at 700–1200 °C to obtain zinc–niobium oxide, and the obtained product was named $Zn_3Nb_2O_8$-A.

3.0 mmol of zinc acetate ($C_4H_6O_4Zn\cdot 2H_2O$, 98%, Aladdin) and 2.0 mmol of niobium oxalate ($C_{10}H_5NbO_{20}$, 98%, Macklin) were added to a mixed solution of 40 mL of H_2O and 20 mL of C_2H_5OH, and stirred vigorously for 2 h (Fig. 1b). The uniformly stirred mixed solution was transferred to a Teflon reactor, and then placed in a blast oven at 180 °C for 24 h. The mixed solution was washed with deionized water and absolute ethanol for several times, dried in a blast drying oven at 80 °C for 12 h, and calcined at high temperature to obtain $Zn_3Nb_2O_8$-B.

2.2 Material characterization

The phase and crystal structure of the as-synthesized materials were analyzed by X-ray diffractometer (XRD, D/MAX-2200). The element information of the as-prepared materials was recorded by X-ray photoelectron spectrometry (XPS, Thermo Scientific K-Alpha). The morphologies of the materials were observed by scanning electron microscope (SEM, Hitachi SU-70) equipped with energy dispersive spectroscopy (EDS). The microstructures of the as-prepared materials were characterized by the transmission electron microscope (TEM, JEOL JEM-2100F).

2.3 Electrochemical measurements

The working electrode consists of 70 wt% active material ($Zn_3Nb_2O_8$), 20 wt% conductive agent Super P, 10 wt% polyvinylidenefluoride (PVDF), and appropriate amount of *N*-methyl-2-pyrrolidone (NMP). Then, the uniformly mixed slurry was coated on copper foil and dried in a vacuum oven at 80 °C for 12 h. The electrodes were assembled into coin-shaped cells (CR2032) using lithium foil as the counter electrode and Whatman glassfiber as the separator. For lithium-ion batteries, the electrolyte was composed of 1.0 mol L^{-1} $LiPF_6$ solution in a mixture (1 : 1 : 1, in vol%) of ethylene carbonate (EC), diethyl carbonate (DEC), and ethyl methyl carbonate (EMC). 1.0 mol L^{-1} $NaPF_6$ in diglyme was used as electrolyte for sodium-ion batteries. The LAND testing system (CT2001A) was used for constant current (dis)charge test and galvanostatic intermittent titration technique (GITT) measurement in the voltage range of 0.01–3.00 V. Electrochemical workstation (CHI 660E) was used to measure cyclic voltammetry (CV) and electrochemical impedance spectroscopy (EIS).

3 Results and discussion

Firstly, the optimal sintering temperature of $Zn_3Nb_2O_8$ materials was investigated. Take $Zn_3Nb_2O_8$-A materials for example, as shown in Fig. S1a,† XRD patterns of the zinc niobate materials that were calcined at 700–1200 °C for 2 h in air. The products are $ZnNb_2O_6$ phase (no. JCPDS 76-1827) and unreacted ZnO precursor in the calcination temperature range from 700 to 850 °C. It is worth mentioning that a strong diffraction peak appears at 30.21°, which is consistent with the characteristic peak of $ZnNb_2O_6$. When the calcination temperature reaches 900 °C, the diffraction peak at 30.21° becomes weaker, but a weaker $Zn_3Nb_2O_8$ diffraction peak appears at 32.72°. When the calcination temperature rises to 950 °C, all diffraction peaks are completely consistent with the diffraction peaks of

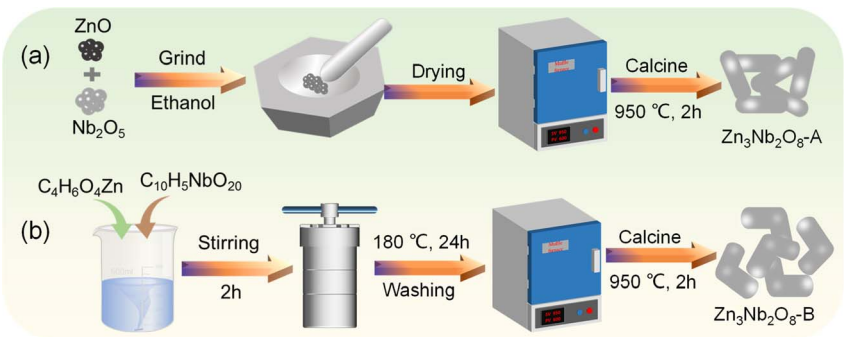

Fig. 1 Schematic illustration of $Zn_3Nb_2O_8$ materials synthesized by (a) solid-state reaction and (b) solvothermal reaction.

monoclinic $Zn_3Nb_2O_8$ (no. JCPDS 79-1164). When the calcination temperature continues to rise to 1000 or 1200 °C, the characteristic peak at 32.72° disappears, and a strong diffraction peak of $ZnNb_2O_6$ appears at 30.21°. In conclusion, the optimum calcination temperature of $Zn_3Nb_2O_8$ is preliminarily determined to be 950 °C. In addition, the effect of precursors in different calcination atmospheres (air or argon) and heating rates on the synthesis of $Zn_3Nb_2O_8$ was investigated, and the XRD patterns of the products are shown in Fig. S1b.† It can be seen that the XRD patterns of the three samples are consistent with the diffraction peaks of monoclinic $Zn_3Nb_2O_8$ (no. JCPDS 79-1164), indicating the successful synthesis of $Zn_3Nb_2O_8$ materials. The ideal calcination setting for $Zn_3Nb_2O_8$ material, however, is calcination to 950 °C at a heating rate of 10 °C min^{-1} under an air atmosphere, taking time and cost into consideration. Based on the above optimal sintering conditions, the XRD spectra of the as-prepared $Zn_3Nb_2O_8$-A and $Zn_3Nb_2O_8$-B are shown in Fig. 2a. It can be seen that the diffraction peaks of both samples correspond to the diffraction peaks of monoclinic $Zn_3Nb_2O_8$, indicating the successful preparation of $Zn_3Nb_2O_8$ materials. Fig. 2b presents the crystal structure of $Zn_3Nb_2O_8$-A and $Zn_3Nb_2O_8$-B, which has a corundum-like monoclinic cell structure (a = 19.093 Å, b = 5.927 Å and c = 5.22 Å), and the space group is $C2/c$. ZnO_6 and NbO_6 have shear-type ReO_3 octahedral structures. There are corner and edge sharing between octahedra to form quadrilateral channels. In addition, the distance between O1 and O3 is 4.31 Å, and the distance between O2 and O4 is 2.94 Å, which can allow the normal insertion and extraction of metal-ion (Li^+ and Na^+).

X-ray photoelectron spectroscopy (XPS) was applied to investigate the element composition and valence state of the material surface. Fig. 2c shows the XPS survey spectra of $Zn_3Nb_2O_8$-B materials, in which the zinc, niobium, oxygen, carbon elements were detected. In the Zn 2p spectra (Fig. 2d), the XPS peaks located at 1021.8 and 1044.9 eV can be attributed to the Zn $2p_{3/2}$ and Zn $2p_{1/2}$ binding energies of Zn^{2+}, respectively.[7] Fig. 2e shows two strong characteristic peaks centered at 207.0 eV and 209.7 eV in the high resolution Nb 3d XPS spectrum, consistent with $3d_{5/2}$ and $3d_{1/2}$, which confirms the presence of Nb^{5+}.[25–27] The O 1s spectrum (Fig. 2f) can be spilt into three peaks at 530.3, 531.8, and 533.0 eV, which were related to the Zn–O/Nb–O, C–O, and C=O, respectively.[28] In the

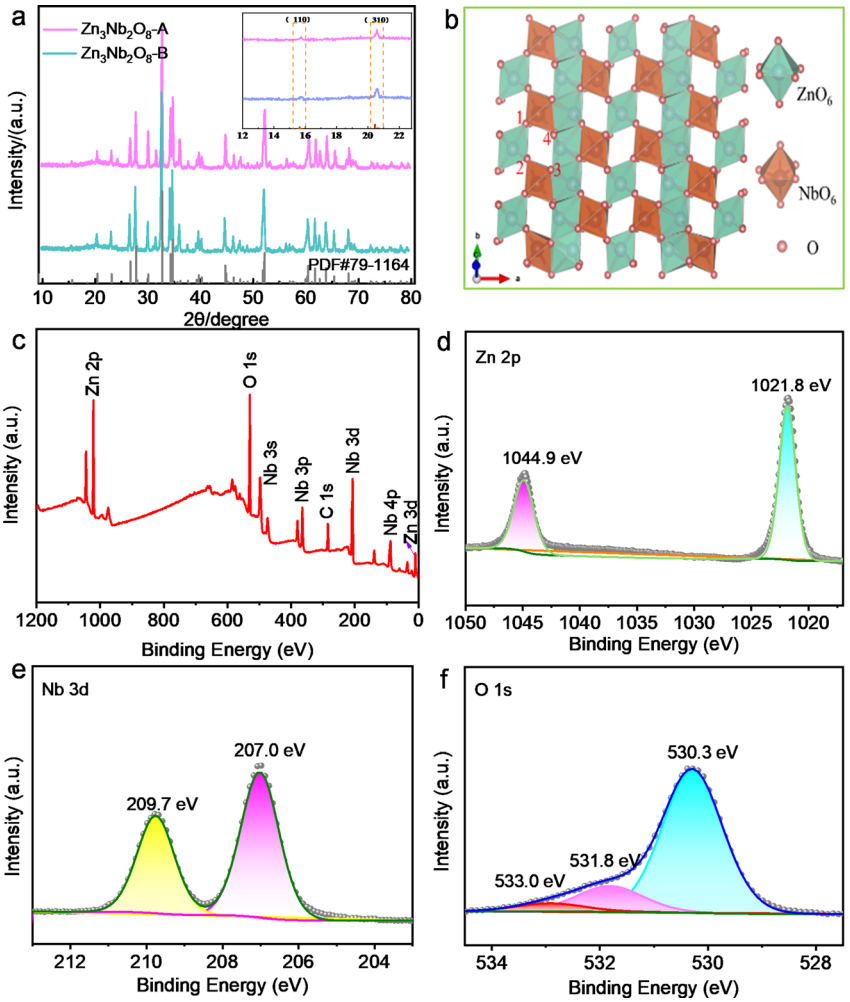

Fig. 2 (a) XRD pattern of $Zn_3Nb_2O_8$-A and $Zn_3Nb_2O_8$-B calcined at 950 °C at 10 °C min^{-1} in air. (b) Crystal structure of $Zn_3Nb_2O_8$, (c) XPS survey spectra of $Zn_3Nb_2O_8$-B; XPS spectra of $Zn_3Nb_2O_8$-B for (d) Zn 2p, (e) Nb 3d, (f) O 1s.

C 1s high-resolution spectrum of $Zn_3Nb_2O_8$-B (Fig. S2†), the peaks at 286.2, 285.3, and 284.8 eV are attributed to C═O, C–O, and C–C groups, respectively.[11] In addition, the XPS spectra of $Zn_3Nb_2O_8$-A are shown in Fig. S3.† These results demonstrate that the valence states of Zn, Nb and O elements in both samples are Zn^{2+}, Nb^{5+} and O^{2-}, respectively.

In order to explore the effect of preparation method on the morphology of $Zn_3Nb_2O_8$, scanning electron microscope (SEM) and elemental mapping characterizations were carried out. Fig. 3a and b shows the SEM images of $Zn_3Nb_2O_8$-A sample, it can be seen that these particles are smooth, with arborescent particle sizes ranging from 300 to 2300 nm. However, $Zn_3Nb_2O_8$-B sample shows a different morphology. As shown in Fig. 3e and f, SEM images clearly show that the $Zn_3Nb_2O_8$-B particles are rough, stump-like, no-aggregating, and the particle size ranges from 250 to 1700 nm. Meanwhile, Fig. 3i demonstrates the energy dispersive spectroscopy (EDS) mapping images of $Zn_3Nb_2O_8$-B, which further confirmed the homogeneous distribution of elements (Zn, Nb, O) in the $Zn_3Nb_2O_8$-B, indicating the $Zn_3Nb_2O_8$ has been successfully synthesized. In addition, the EDS mapping images of $Zn_3Nb_2O_8$-A are presented in Fig. S4,† the uniform homogeneous distribution of elements (Zn, Nb, O) in the $Zn_3Nb_2O_8$-A also proved its successful preparation. The microstructures of $Zn_3Nb_2O_8$-A and $Zn_3Nb_2O_8$-B were confirmed by transmission electron microscope (TEM). As shown in Fig. 3c and d, there are distinct fringes with lattice spacing of about 0.44 nm, corresponding to the (310) facet in $Zn_3Nb_2O_8$-A. In addition, the distances of lattice fringes are measured to be 0.57 nm, corresponding to the (110) facet in $Zn_3Nb_2O_8$-B. Different crystal facets in $Zn_3Nb_2O_8$-A and $Zn_3Nb_2O_8$-B were observed by TEM, indicating that there may be more (110) facet exposure in $Zn_3Nb_2O_8$-B and more (310) facet exposure in $Zn_3Nb_2O_8$-A. Therefore, the area ratio of exposed (110)/(310) facets in $Zn_3Nb_2O_8$-A and $Zn_3Nb_2O_8$-B are roughly calculated based on these XRD pattern in Fig. 2a. The approximate ratios of (110)/(310) facets in $Zn_3Nb_2O_8$-A and $Zn_3Nb_2O_8$-B are 34.2% and 41.2%, respectively. XRD and TEM results show that the area ratio of exposed (110)/(310) facets in $Zn_3Nb_2O_8$-A is lower than that in $Zn_3Nb_2O_8$-B. The lattice spacing of (110) facet is larger than that of (310) facet, so $Zn_3Nb_2O_8$-B material may be more conducive to the rapid insertion and extraction of metal-ions (Li^+ and Na^+).

In order to explore the effect of $Zn_3Nb_2O_8$-A and $Zn_3Nb_2O_8$-B samples on the electrochemical performance, $Zn_3Nb_2O_8$-A/Li and $Zn_3Nb_2O_8$-B/Li half-cells for lithium-ion storage were assembled (Fig. 4a). Fig. 4b shows the cyclic voltammetry (CV)

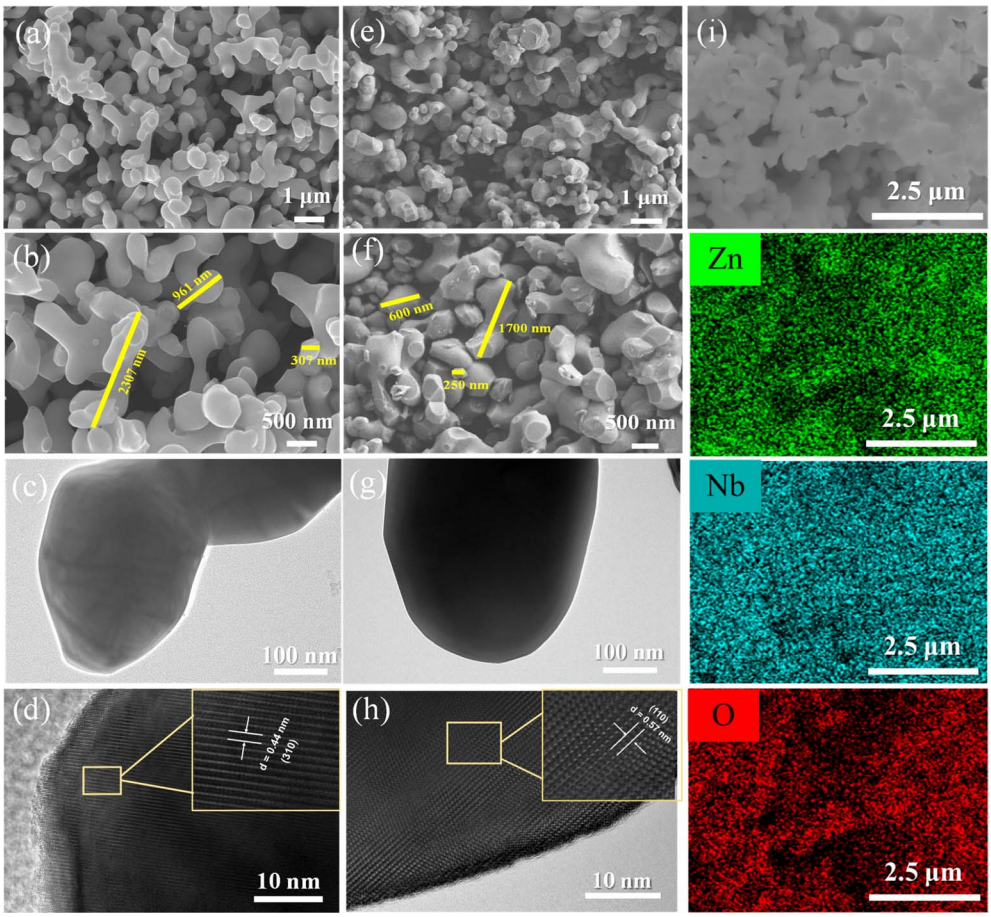

Fig. 3 (a and b) SEM images, (c) TEM image and (d) HRTEM image of $Zn_3Nb_2O_8$-A; (e and f) SEM images, (g) TEM image, (h) HRTEM image and (i) EDS mapping images of $Zn_3Nb_2O_8$-B.

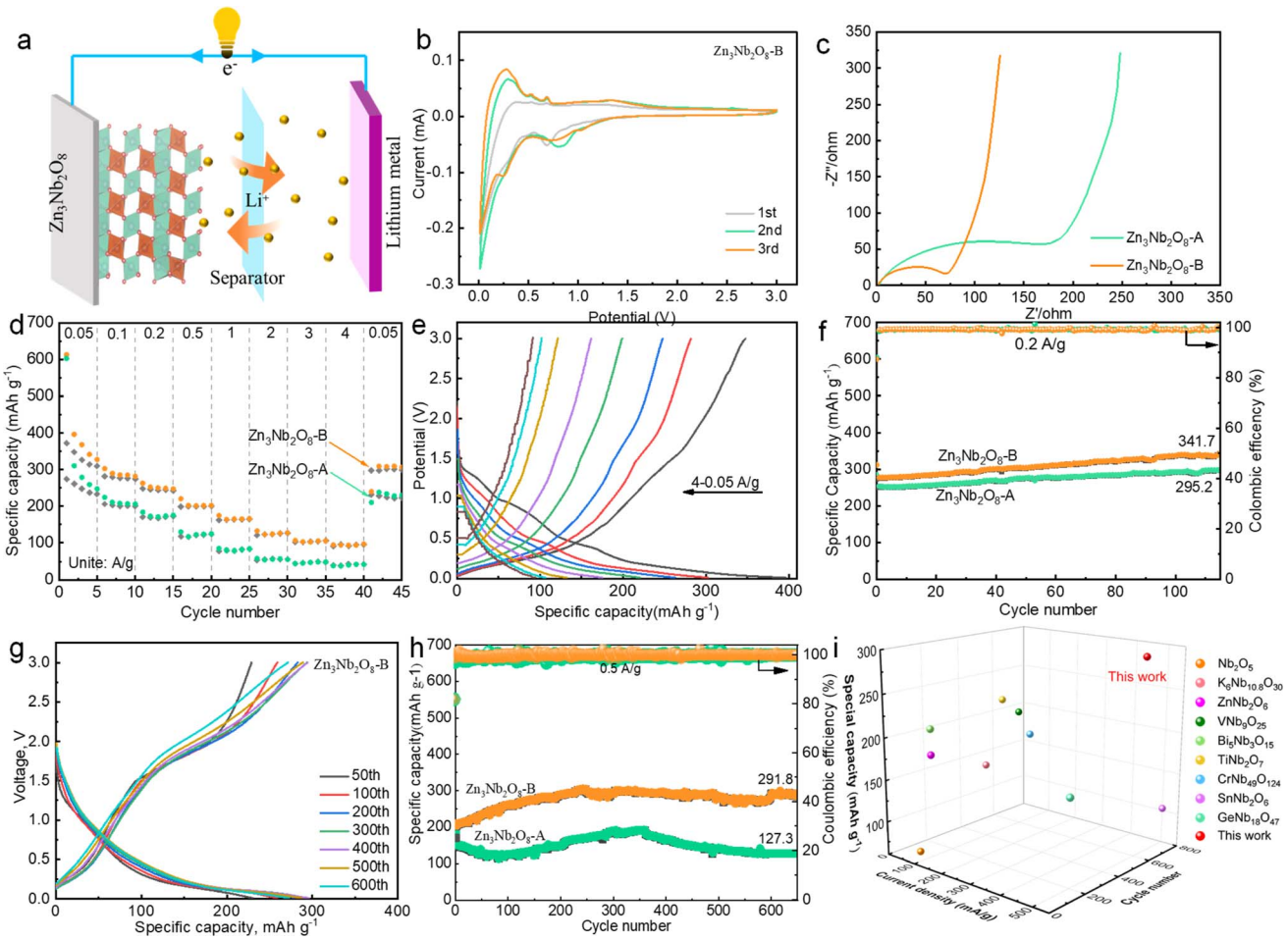

Fig. 4 (a) Schematic illustration of $Zn_3Nb_2O_8$//Li lithium-ion cell. (b) CV curves of $Zn_3Nb_2O_8$-B at the scan rate of 0.1 mV s^{-1}; (c) Nyquist plots of $Zn_3Nb_2O_8$-A and $Zn_3Nb_2O_8$-B; (d) rate performances of $Zn_3Nb_2O_8$-A and $Zn_3Nb_2O_8$-B at different current densities; (e) galvanostatic discharge and charge curves of $Zn_3Nb_2O_8$-B at different current densities from 0.05 to 4.0 A g^{-1}. (f) Cycling performances of $Zn_3Nb_2O_8$ at a current density of 0.2 A g^{-1}; (g) discharge and charge curves of $Zn_3Nb_2O_8$-B at a current density of 0.5 A g^{-1}; (h) cycling performances of $Zn_3Nb_2O_8$ at a current density of 0.5 A g^{-1}. (i) Comparison of cycling stability between $Zn_3Nb_2O_8$-B with other Nb-based anode materials.

curves of $Zn_3Nb_2O_8$-B in the voltage range of 0.01–3.00 V at a scan rate of 0.1 mV s^{-1}. In the cathode process, the broad peaks at the potential of 0.1–0.5 V and 0.5–1.0 V are mainly due to the formation of irreversible SEI and $LixZn_3Nb_2O_8$ products ($Zn_3Nb_2O_8 + xLi^+ + xe^- \leftrightarrow Li_xZn_3Nb_2O_8$).[6,20] In the first anodic process, there is a broad peak at 1.0–1.5 V, which is basically consistent with the subsequent cycle, indicating that the $Zn_3Nb_2O_8$-B material has a good reversibility performance. Additionally, Fig. S5† demonstrates that the CV curves of $Zn_3Nb_2O_8$-A are similar to those of $Zn_3Nb_2O_8$-B.

The Nyquist plots of $Zn_3Nb_2O_8$-A and $Zn_3Nb_2O_8$-B electrode materials show similar curves (Fig. 4c). The charge transfer resistance value of $Zn_3Nb_2O_8$-B is 75 Ω, which is lower than that of $Zn_3Nb_2O_8$-A (230 Ω), indicating that the (110)-exposed $Zn_3Nb_2O_8$-B provided better Li ion/electron transfer kinetics than (310)-exposed $Zn_3Nb_2O_8$-A. It is well known that different surface atoms are arranged according to different crystal facets.[29] This result indicating that the movement of Li ion/electron through the (110) facet is more easily than through the (310) facet of $Zn_3Nb_2O_8$. The rate performance of $Zn_3Nb_2O_8$ electrode was tested at various current densities, as shown in Fig. 4d. The reversible capacities of the $Zn_3Nb_2O_8$-B electrode are 371.8, 282.1, 247.9, 199.1, 161.8, 121.3, 102.1 and 91.4 mA h g^{-1} at current densities of 0.05, 0.10, 0.20, 0.50, 1.00, 2.00, 3.00 and 4.00 A g^{-1}, respectively. The specific capacity returned to 308.1 mA h g^{-1} when the current density was changed back to 0.05 A g^{-1}, revealing the electrode's exceptional structural stability throughout a broad current range. However, the reversible capacities of the $Zn_3Nb_2O_8$-A electrode are relatively low, which are 274.0, 205.9, 170.8, 117.8, 77.8, 53.4, 44.4, 40.1 and 231.3 mA h g^{-1} at current densities of 0.05, 0.10, 0.20, 0.50, 1.00, 2.00, 3.00, 4.00 and 0.05 A g^{-1}, respectively. The corresponding galvanostatic discharge and charge curves of $Zn_3Nb_2O_8$-A and $Zn_3Nb_2O_8$-B at different current densities are shown in Fig. 4e and S6,† it can be seen that the capacity is mainly contributed by the slope segment. In addition, the cycling performance was also investigated at a current density of 0.2 A g^{-1} (Fig. 4f). The $Zn_3Nb_2O_8$-B electrode had a high specific capacity of 341.7 mA h g^{-1} after 115 cycles. While the $Zn_3Nb_2O_8$-A electrode had a relative low specific capacity of

295.2 mA h g^{-1} after 115 cycles. The partial discharge and charge curves of $Zn_3Nb_2O_8$-A and $Zn_3Nb_2O_8$-B electrodes are shown in Fig. S7.† Increasing the current density to 0.5 A g^{-1}, the long-cycling stability of $Zn_3Nb_2O_8$-A and $Zn_3Nb_2O_8$-B electrodes were investigated (Fig. 4h). After 650 cycles, the discharge capacities of $Zn_3Nb_2O_8$-A and $Zn_3Nb_2O_8$-B are 291.8 and 127.3 mA h g^{-1}, respectively, and the corresponding discharge–charge curves are presented in Fig. 4g and S7c.† Obviously, the overall capacity of the electrode material decreases first and then increases during cycling. The initial capacity attenuation is mainly attributed to the fracture and exfoliate of the electrode material during the Li^+ insertion and extraction processes. The subsequent capacity increase is ascribed to the rapid Li-diffusion kinetics in the SEI layer. This similar behavior has been reported in the previous literature.[6,30–32]. Compared with $Zn_3Nb_2O_8$-A materials, $Zn_3Nb_2O_8$-B materials show excellent cycling and rate performance, which may be due to the exposure of (110) facets in $Zn_3Nb_2O_8$-B materials.[33–35] More importantly, as shown in Fig. 4i and Table S1,† the cycling stability of $Zn_3Nb_2O_8$-B was particularly better than that of other Nb-based anode materials (*e.g.* Nb_2O_5, $K_6Nb_{10.8}O_{30}$, $ZnNb_2O_6$, $Bi_5Nb_3O_{15}$, VNb_9O_{25}, $CrNb_{49}O_{124}$, $TiNb_2O_7$, $WNb_{12}O_{33}$ and $GaNb_{18}O_{47}$).

In order to further explore the mechanism for excellent electrochemical performance of $Zn_3Nb_2O_8$-B material. The reaction kinetics and charge storage mechanism of $Zn_3Nb_2O_8$-A and $Zn_3Nb_2O_8$-B were analyzed using CV tests with scanning rates in the range of 0.1–10.0 mV s^{-1} (Fig. S8a† and 5a). The relationship between the peak current i (A) and the scanning rate v (mV s^{-1}) follows the following equation: $i = av^b$. Diffusion-controlled processes are indicated by a b-value of 0.5, whereas surface capacitance-controlled processes are indicated by a b-value of 1.[36] The calculated b-values of $Zn_3Nb_2O_8$-A and $Zn_3Nb_2O_8$-B are shown in Fig. S8b† and 5b, respectively. The b-values of anodic (oxidation) and cathodic (reduction) peaks for $Zn_3Nb_2O_8$-B electrode were calculated to be 0.77 and 0.95. While the $Zn_3Nb_2O_8$-A showed the b-values are 0.69 and 0.78 for the anodic and cathodic (reduction) peaks, respectively. The results indicating that the charge storage mechanism for $Zn_3Nb_2O_8$-A and $Zn_3Nb_2O_8$-B is a combination of surface capacitance-controlled process and diffusion-controlled behavior. However, $Zn_3Nb_2O_8$-B displays a greater b-values than $Zn_3Nb_2O_8$-A and exhibits a pseudo-capacitive tendency. This behavior could enable the fast charge transport.[7] A typical CV curves at 2.0 mV s^{-1} are shown in Fig. S9,† the pseudo-capacitive capacity contribution of $Zn_3Nb_2O_8$-A and $Zn_3Nb_2O_8$-B at different sweep rates are calculated as shown in Fig. 5c and S8d,† respectively. The results demonstrate that the pseudo-capacitance contribution of both electrodes are obviously improving with sweep rates rising, but the capacitance contribution of $Zn_3Nb_2O_8$-B electrode is significantly higher than that of $Zn_3Nb_2O_8$-A electrode at the same sweep rate, indicating that the $Zn_3Nb_2O_8$-B electrode has fast electron/ion transport kinetics, which eventually makes it have good long-term stability.

In addition, the diffusion coefficient of Li^+ in the electrode material is measured by GITT and can be calculated according to the following formula:[37]

$$D = \frac{4}{\pi\tau}\left(\frac{n_B V_M}{S}\right)^2\left(\frac{\Delta E_s}{\Delta E_t}\right)^2 \quad (1)$$

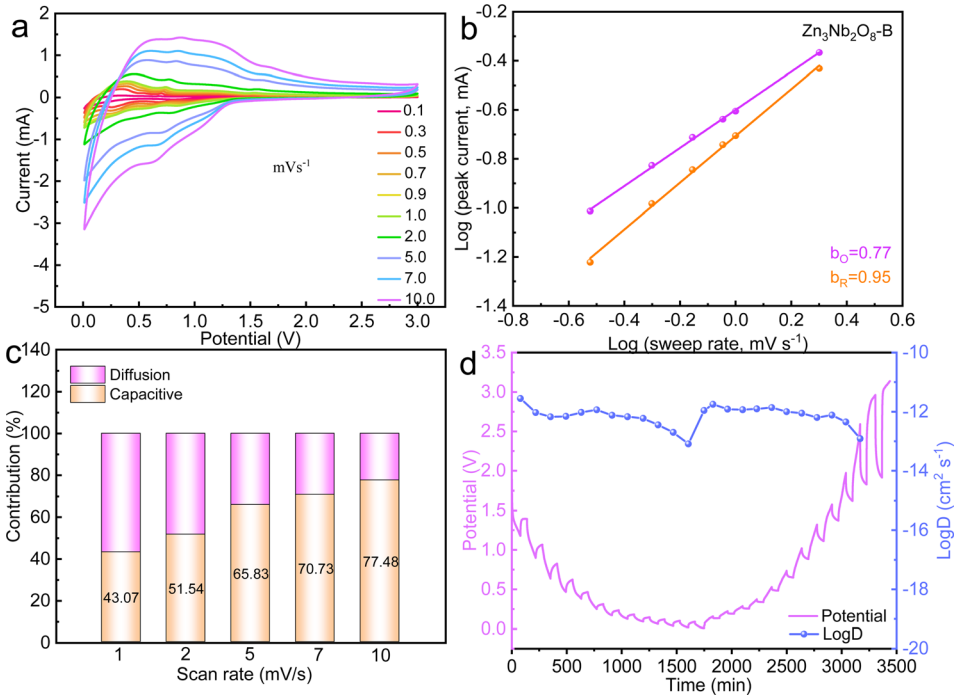

Fig. 5 (a) CV curves of $Zn_3Nb_2O_8$-B from 0.1 to 10.0 mV s^{-1}; (b) plots of log(*i*) *vs.* log(*v*) of the $Zn_3Nb_2O_8$-B/Li cell; (c) contribution ratios of diffusion- and capacitive-controlled capacities at different scan rates. (d) GITT curves of $Zn_3Nb_2O_8$-B at 0.01–3.00 V.

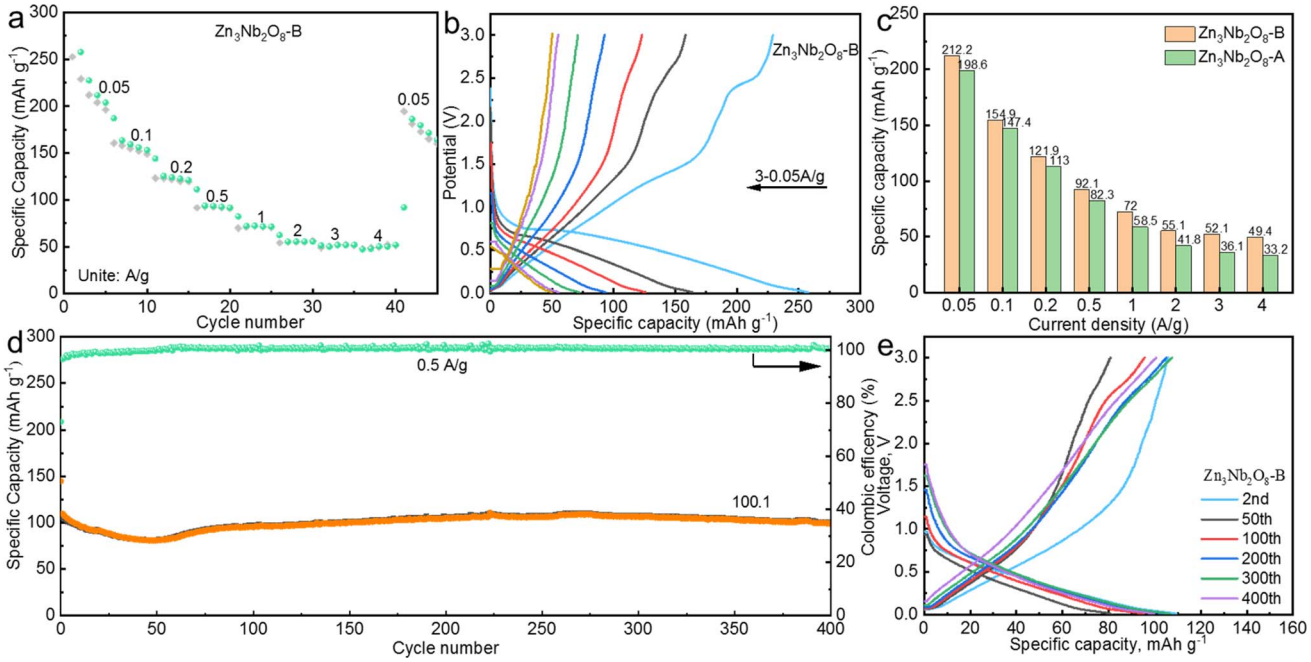

Fig. 6 (a) Rate performances of $Zn_3Nb_2O_8$-B at different current densities for SIBs; (b) galvanostatic discharge and charge curves of $Zn_3Nb_2O_8$-B at different current densities from 0.05 to 3.0 A g^{-1}. (c) Comparison of specific capacities of $Zn_3Nb_2O_8$-A and $Zn_3Nb_2O_8$-B electrodes at different current densities. (d) Cycling performances of $Zn_3Nb_2O_8$-B at a current density of 0.5 A g^{-1}; (e) discharge and charge curves of $Zn_3Nb_2O_8$-B at a current density of 0.5 A g^{-1}.

where τ is the relaxation time, n_B is the number of moles, V_M is the molar volume of the electrode material, S is the electrode/electrolyte contact area, ΔE_s is the voltage change caused by the pulse, and ΔE_t is the constant current (dis)charging voltage changes.

The GITT curves and corresponding D values of $Zn_3Nb_2O_8$-B during the charge–discharge process are shown in Fig. 5d, and the average value of log(D) during the (de)intercalation of Li^+ is $\sim 1 \times 10^{-12}$. The results of EIS and GITT together confirm that Li^+ can diffuse rapidly in the $Zn_3Nb_2O_8$-B electrode material. Therefore, the $Zn_3Nb_2O_8$-B electrode can effectively reduce the charge transfer resistance and accelerate Li^+ migration, resulting in excellent rate performance.

We further investigated the application of $Zn_3Nb_2O_8$-B in sodium-ion batteries, the electrodes were assembled into coin-shaped cells using sodium foil as counter electrode. The rate behaviors of the $Zn_3Nb_2O_8$-B anode throughout a current density range of 0.05 to 4.0 A g^{-1} are shown in Fig. 6a. $Zn_3Nb_2O_8$-B demonstrated good rate performance in comparison to $Zn_3Nb_2O_8$-A (Fig. 6c), producing reversible capacities of 212.2, 154.9, 121.9, 92.1, 72.0, 55.1, 52.1, and 49.4 mA h g^{-1} at current densities of 0.05, 0.1, 0.2, 0.5, 1, 2, 3, and 4 A g^{-1}, respectively. Then, when the current density was decreased to 0.05 A g^{-1}, the specific capacity of the $Zn_3Nb_2O_8$-B anode recovered to 172.9 mA h g^{-1}, demonstrating the good kinetic process. The corresponding discharge and charge curves of $Zn_3Nb_2O_8$-B at different current densities are displayed in Fig. 6b. As a comparison of $Zn_3Nb_2O_8$-A electrode, the rate performance and discharge–charge curves at different current densities are shown in Fig. S10a and b.† In addition, Fig. 6d displays the long cycle stability of $Zn_3Nb_2O_8$-B electrode at 0.5 A g^{-1}, the discharge capacity of $Zn_3Nb_2O_8$-B is 100.1 mA h g^{-1} with 94.5% capacity retention after 400 cycles. While the $Zn_3Nb_2O_8$-A electrode has a relative low specific capacity of 50.8 mA h g^{-1} with 61.3% capacity retention after 400 cycles (Fig. S10c†). Compared with $Zn_3Nb_2O_8$-A electrode, the better electrochemical performance of $Zn_3Nb_2O_8$-B electrode may be related to the exposed (110) crystal planes, which enables more sodium-ions to be (de)intercalated. As shown in Fig. S11,† the EIS demonstrated that the impedance of $Zn_3Nb_2O_8$-A (12.7 Ω) is significantly higher than that of $Zn_3Nb_2O_8$-B (10.7 Ω), which indicated that $Zn_3Nb_2O_8$-B has a fast charge transfer rate. Based on the above tests and analysis show that $Zn_3Nb_2O_8$-B can be used as an excellent negative electrode for LIBs/SIBs.

4 Conclusions

In summary, we have successfully designed $Zn_3Nb_2O_8$-A and $Zn_3Nb_2O_8$-B anode materials *via* solid-state reaction and solvothermal methods, respectively. SEM results show that $Zn_3Nb_2O_8$-A particles were arborescent and smooth, while the $Zn_3Nb_2O_8$-B particles were stump-like and rough. XRD and TEM results show that the area ratio of exposed (110)/(310) facets in $Zn_3Nb_2O_8$-A is lower than that in $Zn_3Nb_2O_8$-B, the (110) facet is more conducive to the rapid insertion and extraction of metal-ions (Li^+ and Na^+) than (310) facet. Compared with the $Zn_3Nb_2O_8$-A anode material, the $Zn_3Nb_2O_8$-B anode material exhibits superior long-cycle cyclability and better rate performance. It displays a high reversible specific capacity of

291.8 mA h g^{-1} at the current density of 0.5 A g^{-1} after 650 cycles and a large reversible specific capacity of 91.4 mA h g^{-1} at 4.0 A g^{-1} in Li-ion batteries. In addition, $Zn_3Nb_2O_8$-B electrode exhibits excellent reversible specific capacity of 100.1 mA h g^{-1} at the current density of 0.5 A g^{-1} after 400 cycles in sodium-ion batteries. This work provides an effective strategy for the application in high performance lithium/sodium energy storage.

Data availability

Data are available on request from the authors.

Author contributions

Xuemin Yin: experimental work, writing the original draft, and reviewing the draft. Shuling Cheng: conceptualization, experimental work, data analysis. Yuyang Zhang: conceptualization, formal analysis. Chencheng Liu: conceptualization.

Conflicts of interest

The authors declare no competing interest.

Acknowledgements

The authors are grateful for the financial support from the Science Research Project of Hebei Education Department (BJK2024063), Open Foundation of Hebei Key Laboratory of Green Development of Rock and Mineral Materials (RM202305).

References

1 J. Chen, Y. Yang, S. Yu, Y. Zhang, J. Hou, N. Yu and B. Fang, *Nanomaterials*, 2023, **13**, 2416.
2 C. Sun, Y.-J. Wang, D. Liu, B. Fang, W. Yan and J. Zhang, *Chem. Eng. J.*, 2023, **453**, 139603.
3 B. Fang, Y.-J. Wang and H. Wang, *Matter*, 2023, **6**, 2508.
4 M. Huang, J. X. Liu, P. Huang, H. Hu and C. Lai, *Rare Met.*, 2021, **40**, 425.
5 R. Zheng, Y. Li, H. Yu, T. Liu, M. Xia, X. Zhang, N. Peng, J. Zhang, Y. Bai and J. Shu, *Chem. Eng. J.*, 2020, **384**, 123314.
6 X. F. Li, J. Li, R. N. Ali, Z. Wang, G. J. Hu and B. Xiang, *Chem. Eng. J.*, 2019, **368**, 764.
7 X. Zhu, H. Cao, R. Li, Q. Fu, G. Liang, Y. Chen, L. Luo, C. Lin and X. S. Zhao, *J. Mater. Chem. A*, 2019, **7**, 25537.
8 Y. Yuan, H. Yu, X. Cheng, R. Zheng, T. Liu, N. Peng, N. Long, M. Shui and J. Shu, *Chem. Eng. J.*, 2019, **374**, 937.
9 X. Cheng, Y. Zhao, A. Lushington, J. Gao, Q. Li, P. Zuo, B. Wang, Y. Gao and Y. Ma, *Nano Energy*, 2017, **34**, 15.
10 Q. Tian, W. Ye, H. Yu, X. Cheng, H. Zhu, N. Long, M. Shui and J. Shu, *Ceram. Int.*, 2019, **45**, 1893.
11 L. Yan, J. Shu, C. Li, X. Cheng, H. Zhu, H. Yu, C. Zhang, Y. Zheng, Y. Xie and Z. Guo, *Energy Storage Mater.*, 2019, **16**, 535.
12 S. L. Cheng, X. P. Yin, S. Sarkar, Z. W. Wang, Q. A. Huang, J. J. Zhang and Y. F. Zhao, *Rare Met.*, 2022, **81**, 2645.
13 X. Ma, P. Chen, M. Qian, D. Wu, J. Du, X. Chen, R. Dai, M. Sha, Z. Zi and J. Dai, *J. Alloys Compd.*, 2021, **864**, 158379.
14 J. Wu, G. Pan, W. Zhong, L. Yang, S. Deng and X. Xia, *J. Colloid Interface Sci.*, 2020, **562**, 511.
15 C. Xiao, M. Xia, W. Ye, X. Zhang, S. Chen, H. Yu, W. Bi, M. Shui and J. Shu, *Ceram. Int.*, 2020, **46**, 15527.
16 F. Ran, X. Cheng, H. Yu, R. Zheng, T. Liu, X. Li, N. Ren, M. Shui and J. Shu, *Electrochim. Acta*, 2018, **282**, 634.
17 S. N. He, Y. L. Xu, X. N. Ma, Y. J. Chen, J. Lin and C. Wang, *ChemElectroChem*, 2020, **7**, 2087.
18 S. Qian, H. Yu, L. Yan, H. Zhu, X. Cheng, Y. Xie, N. Long, M. Shui and J. Shu, *ACS Appl. Mater. Interfaces*, 2017, **9**, 30608.
19 X. Zhu, Q. Fu, L. Tang, C. Lin, J. Xu, G. Liang, R. Li, L. Luo and Y. Chen, *ACS Appl. Mater. Interfaces*, 2018, **10**, 23711.
20 P. Hei, S. Luo, K. Wei, J. Zhou, Y. Zhao and F. Gao, *ACS Sustain. Chem. Eng.*, 2020, **9**, 216.
21 H. Dai, G. Zhang, D. Rawach, C. Fu, C. Wang, X. Liu, M. Dubois, C. Lai and S. Sun, *Energy Storage Mater.*, 2021, **34**, 320.
22 C. P. Lv, C. F. Lin and X. S. Zhao, *Adv. Energy Mater.*, 2021, **12**, 2102550.
23 A. Prasatkhetragarn, R. Yimnirun and S. Ananta, *Mater. Lett.*, 2007, **61**, 3873.
24 P. Pakawanit, P. Amonpattaratkit, R. Yimnirun and S. Ananta, *Ferroelectr. Lett.Sect.*, 2013, **40**, 85.
25 T. Liu, X. Yin, X. Yin, S. Cheng, X. Wang and Y. Zhao, *Chem.–Asian J.*, 2022, **17**, e202200288.
26 S. L. Cheng, X. P. Yin, S. Sarkar, Z. W. Wang, Q. A. Huang, J. J. Zhang and Y. F. Zhao, *Rare Met.*, 2022, **41**, 2645.
27 X. Yin, T. Liu, X. Yin, X. Feng, Y. Liu, Q. Shi, X. Zou and Y. Zhao, *Chin. Chem. Lett.*, 2023, **34**, 107840.
28 G.-Y. Liu, Y.-Y. Zhao, Y.-F. Tang, X.-D. Liu, M. Liu and P.-J. Wu, *Rare Met.*, 2020, **39**, 1063.
29 S. Lee, H. Kim, J.-H. Lee, B.-K. Kim, H. Shin, J. Kim and S. Park, *Nano Energy*, 2021, **79**, 105480.
30 H. Sun, G. Xin, T. Hu, M. Yu, D. Shao, X. Sun and J. Lian, *Nat. Commun.*, 2014, **5**, 4526.
31 D. Li, X. Li, S. Wang, Y. Zheng, L. Qiao and D. He, *ACS Appl. Mater. Interfaces*, 2014, **6**, 648.
32 J. Zhu, Z. Yin, D. Yang, T. Sun, H. Yu, H. E. Hoster, H. H. Hng, H. Zhang and Q. Yan, *Energy Environ. Sci.*, 2013, **6**, 987.
33 Y. Jian, H. Liu, J. Zhu, Y. Zeng, Z. Liu, C. Hou and S. Pu, *RSC Adv.*, 2020, **10**, 42860.
34 Q. Li, T. Li, S. Chang, Q. Tao, B. Tian and J. Zhang, *CrystEngComm*, 2016, **18**, 5074.
35 H. Xu, P. Reunchan, S. Ouyang, H. Tong, N. Umezawa, T. Kako and J. Ye, *Chem. Mater.*, 2013, **25**, 405.
36 Z. Tong, S. Liu, Y. Zhou, J. Zhao, Y. Wu, Y. Wang and Y. Li, *Energy Storage Mater.*, 2018, **13**, 223.
37 X. Wang, X. Yin, X. Feng, Y. Li, X. Dong, Q. Shi, Y. Zhao and J. Zhang, *Chem. Eng. J.*, 2021, **428**, 130990.